Lecture 9: Instabilities, Solar Flares and CMEs

MHD Instabilities

Equilibria could be unstable: when a small perturbation grows:

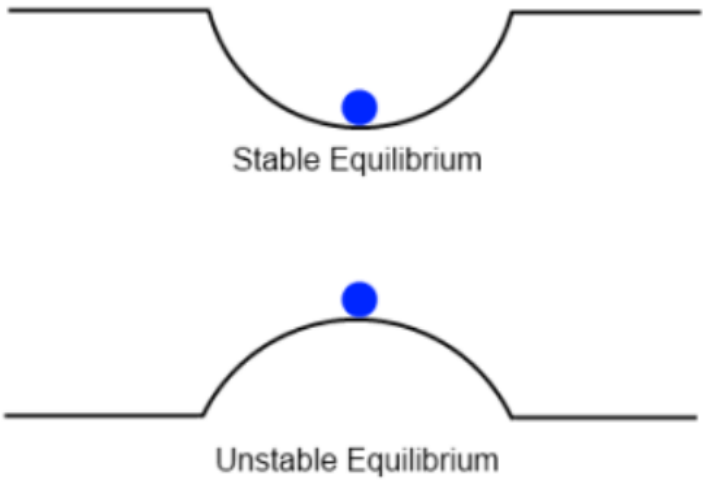

An (incomplete) list of plasma instabilities:

- Bennett pinch instability (also called the z-pinch instability)
- Beam acoustic instability
- Bump-in-tail instability
- Buneman instability,[2] (same as Farley-Buneman instability?)
- Cherenkov instability,[3]
- Chute instability
- Coalescence instability,[4]
- Collapse instability
- Counter-streaming instability
- Cyclotron instabilities, including:
  - Alfven cyclotron instability
  - Electron cyclotron instability
  - Electrostatic ion cyclotron Instability
  - Ion cyclotron instability
  - Magnetoacoustic cyclotron instability
  - Proton cyclotron instability
  - Nonresonant Beam-Type cyclotron instability
  - Relativistic ion cyclotron instability
  - Whistler cyclotron instability
- Diocotron instability,[5] (similar to the Kelvin-Helmholtz fluid instability).
- Disruptive instability (in tokamaks)
- Double emission instability
- Drift wave instability
- Edge-localized modes [2]
- Electrothermal instability
- Farley-Buneman instability
- Fan instability
- Filamentation instability
- Firehose instability (also called Hose instability)
- Flute instability
- Free electron maser instability
- Gyrotron instability
- Helical instability (helix instability)
- Helical kink instability
- Hose instability (also called Firehose instability)
- Interchange instability
- Ion beam instability
- Kink instability
- Lower hybrid (drift) instability (in the Critical ionization velocity mechanism)
- Magnetic drift instability
- Modulation instability
- Non-Abelian instability (see also Chromo-Weibel instability)
- Chromo–Weibel instability
- Non-linear coalescence instability
- Oscillating two stream instability, see two stream instability
- Pair instability
- Parker instability (magnetic buoyancy instability)
- Peratt instability (stacked toroids)
- Pinch instability
- Sausage instability
- Slow Drift Instability
- Tearing mode instability
- Two stream instability
- Weak beam instability
- Weibel instability
- z-pinch instability, also called Bennett pinch instability

Violent instabilities of plasma equilibria occurring in the configuration space — causing a major reconstruction of the plasma configuration —

are known as "macro-instabilities" or "MHD-instabilities". They may be responsible for triggering impulsive energy releases in natural and laboratory plasmas.

A spectacular example of such an instability is a coronal mass ejection (CME) observed in the solar corona.

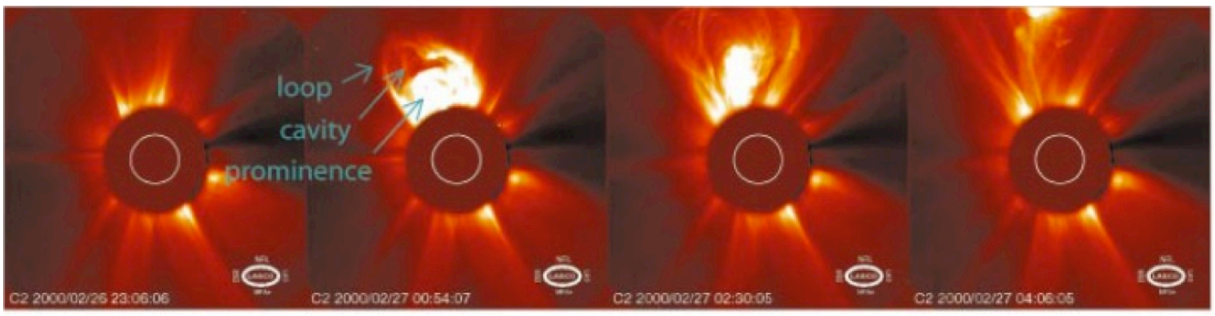

Snapshots of the development of a mass ejection observed in the corona of the Sun from the ESA Solar and Heliospheric Observatory (SoHO) spacecraft. The bright regions correspond to the dense plasma highlighted by the solar light by the effect of Thomson scattering. The sequence of images shows the major reconstruction of the plasma configuration, accompanied by the emergence of a plasma blob. There are several plasma instabilities determining this process and its observational manifestation.

Analysis of MHD instabilities begins usually from the consideration of linear dispersion relations of small perturbations of magnetostatic equilibria, and includes several steps:

- Determine the equilibrium with the use of the magnetostatic equation (the balance of forces);
- Linearise MHD equations with respect to this equilibrium;
- Assume the harmonic dependence on time and the position vector, $\propto \exp(-i\omega t + i\mathbf{k}.\mathbf{r})$;
- If for certain values of $\mathbf{k}$ the imaginary part of the frequency ω is positive, perturbations with those $\mathbf{k}$ are linearly unstable.

For example, for the radiatively unstable plasma we have discussed, the dispersion relation is

$$\omega^2 - C_s^2 k^2 - \frac{ik^2}{\omega}\mathcal{A} = 0, \tag{1}$$

where

$$\mathcal{A} = (\gamma - 1)\left[\left(\frac{\partial \mathcal{L}}{\partial P}\right)_{\text{at equilib}} + C_s^2\left(\frac{\partial \mathcal{L}}{\partial \rho}\right)_{\text{at equilib}}\right].$$

with $\mathcal{L}$ being the radiative cooling and heating function.

For $\mathrm{Im}(\omega) \ll \mathrm{Re}(\omega)$, we obtain

$$\mathrm{Re}(\omega)^2 + 2i\mathrm{Re}(\omega)\mathrm{Im}(\omega) - C_s^2 k^2 - \frac{ik^2}{\mathrm{Re}(\omega)}\mathcal{A} \approx 0,$$

and, separating the real and imaginary parts,
$\mathrm{Re}(\omega)^2 \approx C_s^2 k^2$ — the sound wave,
and $\mathrm{Im}(\omega) \approx \mathcal{A}/C_s^2$. Thus, the condition for the instability is $\mathcal{A} > 0$.

If this condition is fulfilled, an acoustic oscillation increases in time — **thermal overstability**.

The growth time t_{growth} of these perturbations can be obtained from $\mathrm{Im}(\omega)$,

$$e^{-i\omega t} = e^{-i(i\mathrm{Im}(\omega))t} = e^{\mathrm{Im}(\omega)t} = e^{t/t_{\text{growth}}}.$$

Another example: **Rayleigh–Taylor instability**
If a dense plasma layer overlaying a less dense plasma layer, and we account for gravity:

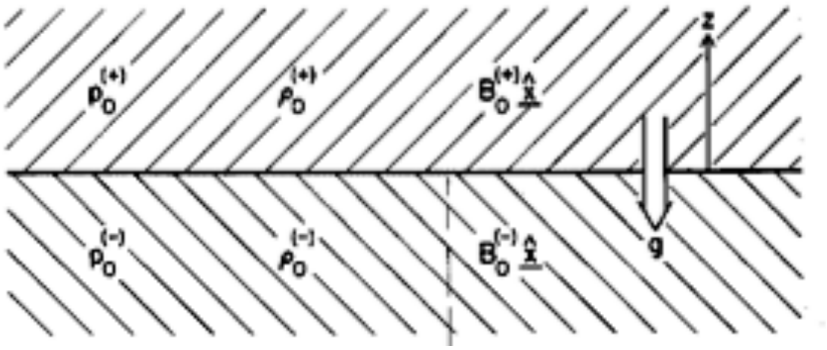

If the magnetic field is vertical, $\mathbf{B}_0 || \mathbf{z}$, dispersion relation is

$$\omega^2 = -gk\frac{\rho_0^{(+)} - \rho_0^{(-)}}{\rho_0^{(+)} + \rho_0^{(-)}}. \tag{2}$$

- Unstable if $\rho_0^{(+)} > \rho_0^{(-)}$.
- Fastest growing perturbations for $k \to \infty$ (small scale).

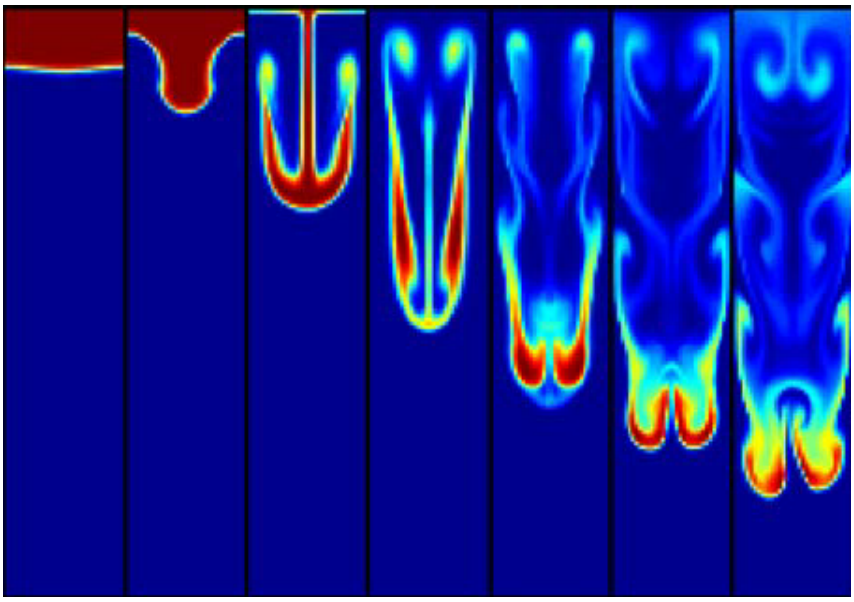

If the magnetic field is horizontal, $\mathbf{B}_0||\mathbf{z}$, dispersion relation is

$$\omega^2 = -gk\frac{\rho_0^{(+)} - \rho_0^{(-)}}{\rho_0^{(+)} + \rho_0^{(-)}} + \frac{2B_0^2 k_x^2}{\mu(\rho_0^{(+)} + \rho_0^{(-)})}. \tag{3}$$

- No effect if $\mathbf{k} \perp \mathbf{B}_0$;
- If $k = k_x$, instability only if $k < k_{\rm crit}$, where

$$k_{\rm crit} = \frac{g\mu(\rho_0^{(+)} - \rho_0^{(-)})}{2B_0^2}$$

is the *threshold of instability.*

- The magnetic tension suppresses the instability: only long-wavelength perturbations are unstable.
- By the way, if $g = 0$ and $\rho_0^{(+)} = \rho_0^{(-)}$, Eq. (3) describes Alfvén waves, $\omega^2 = C_A^2 k_x^2$.

Effect of the magnetic field direction:

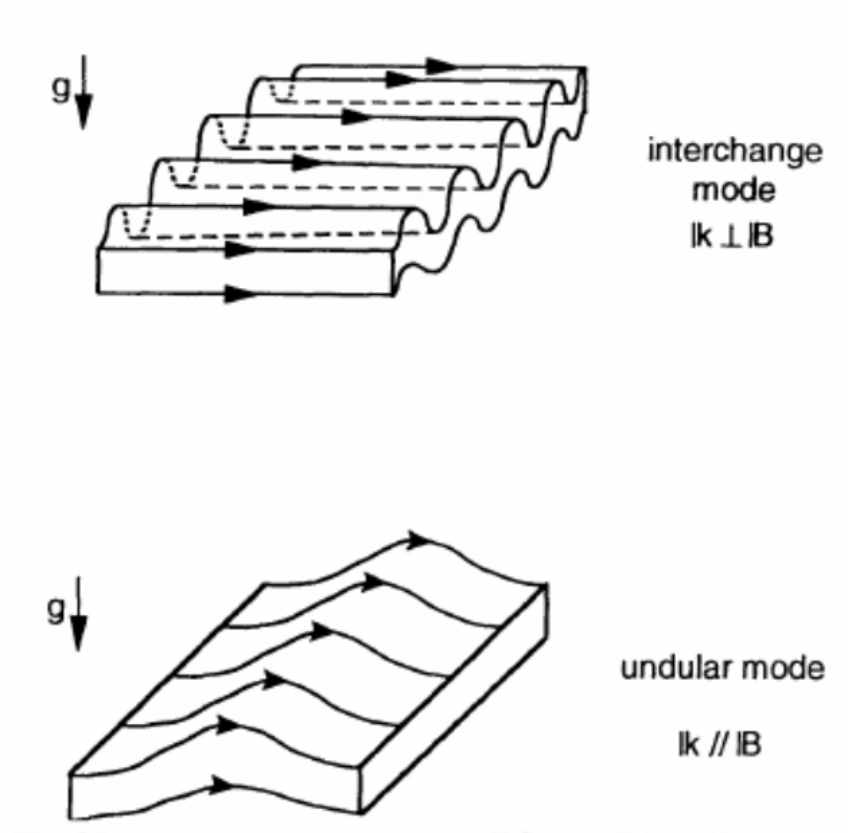

Special case: magnetic layer under a plasma without the field:

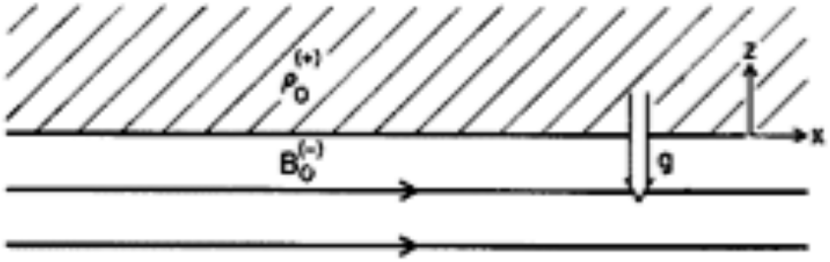

$$\omega^2 = -gk + \frac{k_x^2 B_0^{(-)2}}{\mu \rho_0^{(+)}}$$

The most unstable case is with $k_x = 0$ (i.e. $\mathbf{k} \perp \mathbf{B}_0^{(-)}$), $\mathrm{Im}(\omega) = (gk)^{1/2}$.

The Rayleigh–Taylor instability that appears when a denser plasma is accelerated in a more rarified plasma, e.g. in the laser plasma confinement experiments.

Kelvin–Helmholtz instability

Consider two incompressible fluids separated by a plane ($z = 0$) infinitely sharp interface (a tangential discontinuity). The upper ($z > 0$) and lower ($z < 0$) fluids have different densities, ρ_1 and ρ_2. The upper fluid moves in the x-direction at a constant speed U_0. Let us neglect perturbations in the third direction, $\partial/\partial y = 0$. The gravity is in the z-direction

The dispersion relation is

$$\omega = \frac{kU_0\rho_1 \pm i\sqrt{k^2U_0^2\rho_1\rho_2 - kg(\rho_2 - \rho_1)(\rho_1 + \rho_2)}}{\rho_1 + \rho_2} \tag{4}$$

Side results: $U_0 = 0$,

$$\omega = \pm\frac{\sqrt{kg(\rho_2^2 - \rho_1^2)}}{\rho_1 + \rho_2},$$

interfacial gravity waves for $\rho_1 < \rho_2$ (c.f. the case of Rayleigh–Taylor instability).

If, in addition, $\rho_1 = 0$, $\omega = \pm\sqrt{gk}$ — **surface gravity waves**.

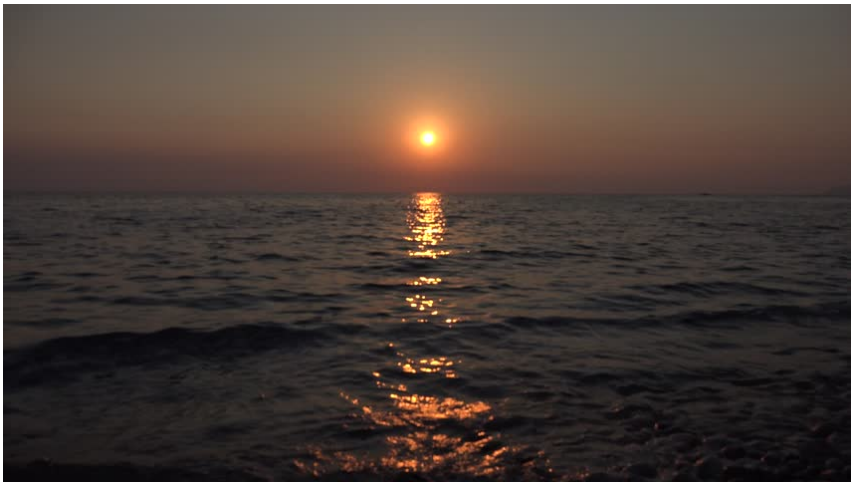

For $U_0 > 0$ — unstable when the argument of the square root is positive, with the threshold

$$U_0^2 = \frac{g(\rho_2^2 - \rho_1^2)}{k\rho_1\rho_2}.$$

In a more general case the KH instability threshold is determined by the compressibility of the medium, direction between the magnetic field and the perturbation vector, and the width of the tangential discontinuity.

Magnetic rope instabilities

As another example, consider macroscopic instability of a very common configuration of a plasma, a *plasma pinch*. In the simplest case, it is a plasma cylinder of a radius a, embedded in vacuum, with an electric current along the axis of the cylinder:

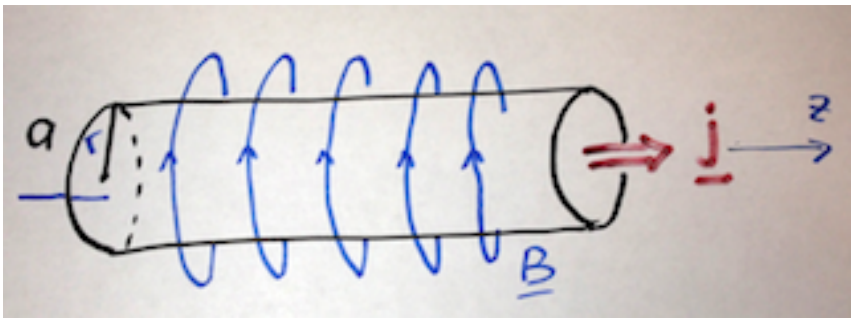

In solar physics, we usually call it a "magnetic rope" — a coherent toroidal magnetic structure with field-lines twisted around its major axis:

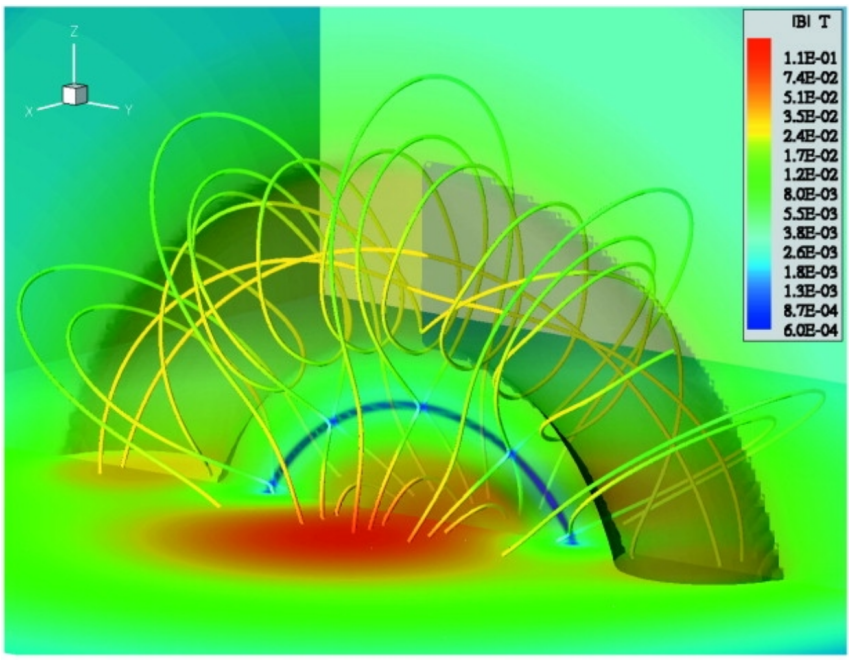

It convenient to describe this configuration in cylindrical coordinates (r, θ, z), with the axis z coinciding with the axis of the cylinder. Consider the case of a uniform electric current inside the cylinder. The current density is given by the expression

$$\mathbf{j} = \begin{cases} (0, 0, j), & r < a, \\ (0, 0, 0), & r > a. \end{cases} \tag{5}$$

The total current inside the plasma pinch is the integral of the current density over the cross-sectional area, $I = \pi a^2 j$. This current creates the magnetic field around the cylinder, and also inside it. In MHD, the current density and magnetic field are connected as $\mathbf{j} = \nabla \times \mathbf{B}/\mu_0$. The symmetry of the problem suggests that $\mathbf{B} = (0, B_\theta(r), 0)$. Thus,

$$\mathbf{j} = \left(0, 0, \frac{1}{\mu_0 r}\frac{d}{dr}(rB_\theta)\right), \tag{6}$$

where we used the expression of the curl in cylindrical coordinates. Thus, we get

$$\frac{1}{\mu_0 r}\frac{d}{dr}(rB_\theta) = \begin{cases} j, & r < a, \\ 0, & r > a, \end{cases} \quad \text{and, hence, } B_\theta = \begin{cases} \frac{\mu_0}{2} jr, & r < a, \\ \frac{\mu_0 a^2}{2r} j, & r > a. \end{cases} \tag{7}$$

This is an equilibrium plasma configuration (see Problems): the plasma is confined ("pinched") to the cylinder by the force created by the magnetic field, generated by the axial current. The magnetic forces counteract the gas pressure force that tries to spread the plasma in the radial direction. But, is such a configuration stable?

Consider an axisymmetric ("sausage") perturbation of the equilibrium, that makes a localised compression of the cylinder (see Fig. 1, upper panel). Let us call the region of the localised compression a "neck". As the electric current at each position along the cylinder should be constant, and as the current is given by the product of the local current density and the cross-sectional area of the cylinder, in the neck the current density must be increased. The increased current density produces the increased magnetic field, $B_\theta = \mu_0 aj/2$. The increased magnetic field causes increased magnetic tension (as the radius of curvature of the field in the neck is smaller) squeezes the plasma in the neck (the frozen-in effect). The compression of the plasma causes the increase in the gas pressure. As the gas pressure is isotropic, its increase in the neck pushes the plasma along the axis of the cylinder along the field. The field-aligned flows remove the plasma from the neck. Thus there is nothing left in the neck to counteract the magnetic forces squeezing it. The perturbation increases and is not stopped. Thus, the equilibrium is unstable to such a perturbation, and the plasma pinch is rapidly destroyed. This effect is known as a "sausage" instability of the plasma pinch.

Moreover, the plasma pinch is also unstable to another perturbation, that is the displacement of the axis of the cylinder ("kink" perturbation, see Fig. 1,

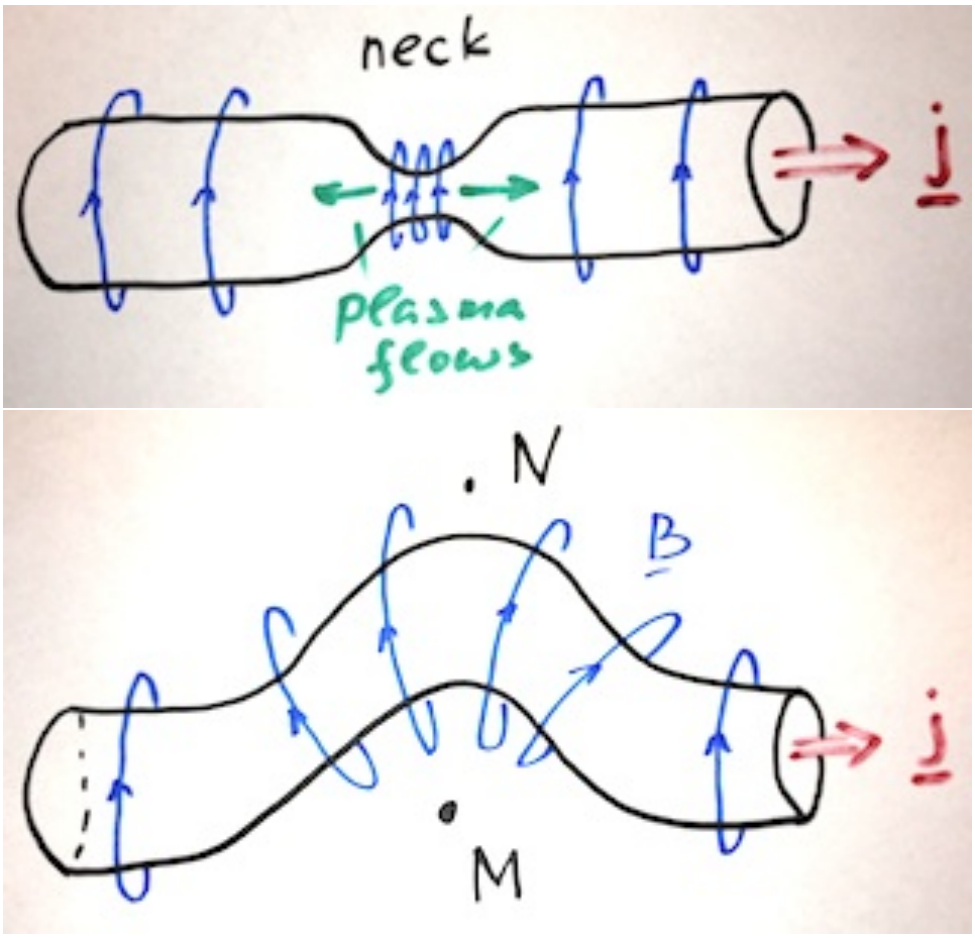

Figure 1: Sketches of a the physical processes in a plasma pinch, that cause the sausage (the upper panel) and kink (the bottom panel) instabilities.

bottom panel). The perturbation makes the magnetic field at the point M stronger (by the absolute value that is the "density" of the magnetic field lines in the sketch) than at the point N. Thus, the magnetic pressure at M is higher than at N, that causes a force that amplifies the perturbation. The perturbation is unbalanced by any forces and hence destroys the plasma configuration. This is the "kink" instability, see Fig. 2.

The consider kink instability is linearly polarised. There could also be a helical kink instability:

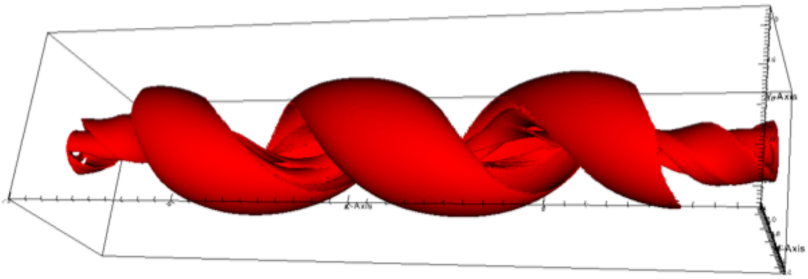

The plasma pinch considered above can be stabilised by adding a magnetic field along the axis of the cylinder.

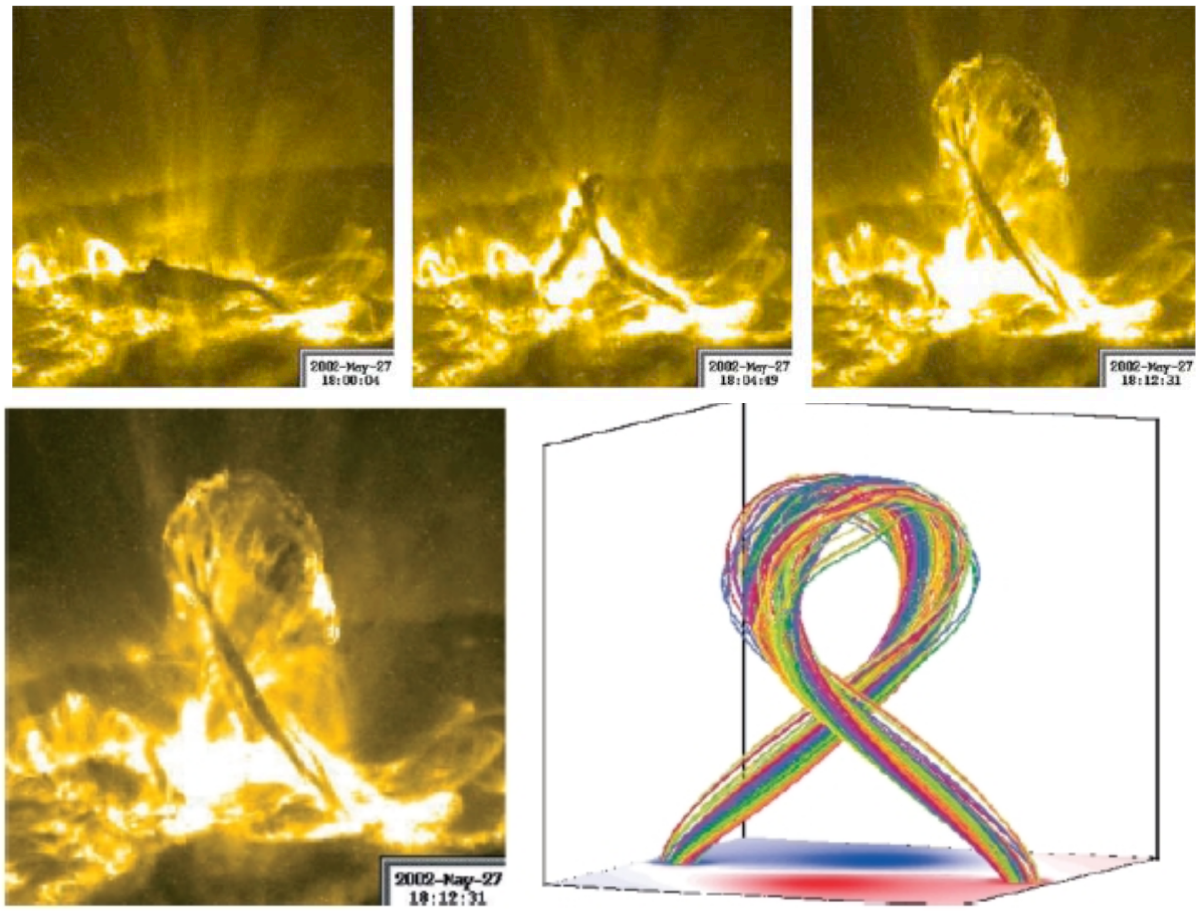

Figure 2: Development of kink instability of a plasma loop in the corona of the Sun, recorded in the EUV band with the Transition Region and Coronal Explorer (TRACE).

Solar Flares

Solar flares are sudden localised brightening in the solar atmosphere, seen in all bands of the solar EM emission, from radio to 100 MeV. The amount of the released energy reaches 10^{27} J.

Time history of a typical flare:

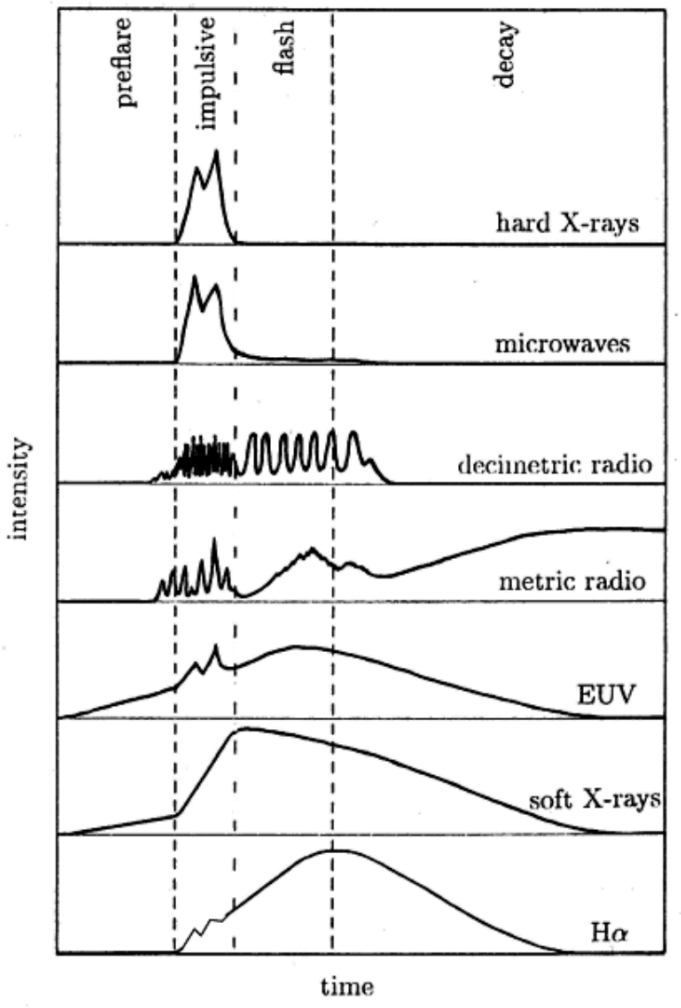

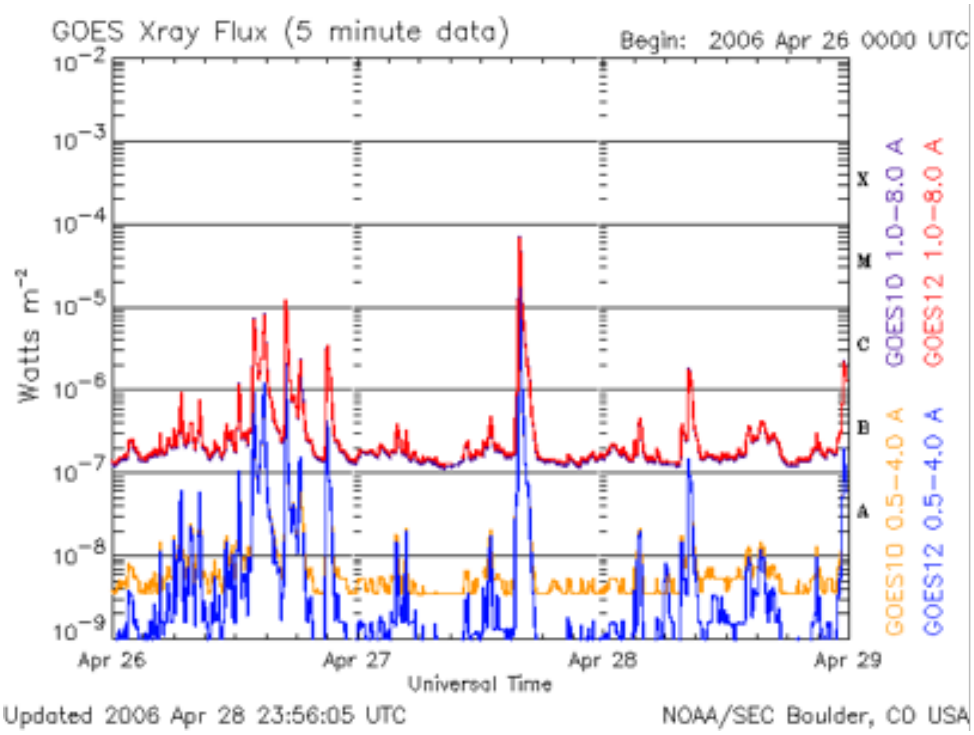

Variation of the soft X-ray flux of the Sun measured by the GOES spacecraft. The spikes correspond to solar flares of different strength.

Classification of solar flares:

Hα classification			Radio flux at 5000 MHz (s.f.u.)	Soft X-ray class	
Importance Class	Area (Sq. deg.)	Area 10^{-6} solar disk		Importance class	Peak flux in 1-8 Å (W/m^2)
S	2.0	200	5	A	10^{-8} to 10^{-7}
1	2.0–5.1	200–500	30	B	10^{-7} to 10^{-6}
2	5.2–12.4	500–1200	300	C	10^{-6} to 10^{-5}
3	12.5–24.7	1200–2400	3000	M	10^{-5} to 10^{-4}
4	>24.7	>2400	3000	X	$>10^{-4}$

(Here s.f.u. is the standard flux unit, corresponding to the radio flux of the quiet Sun).

Composite energy spectrum from a large flare:

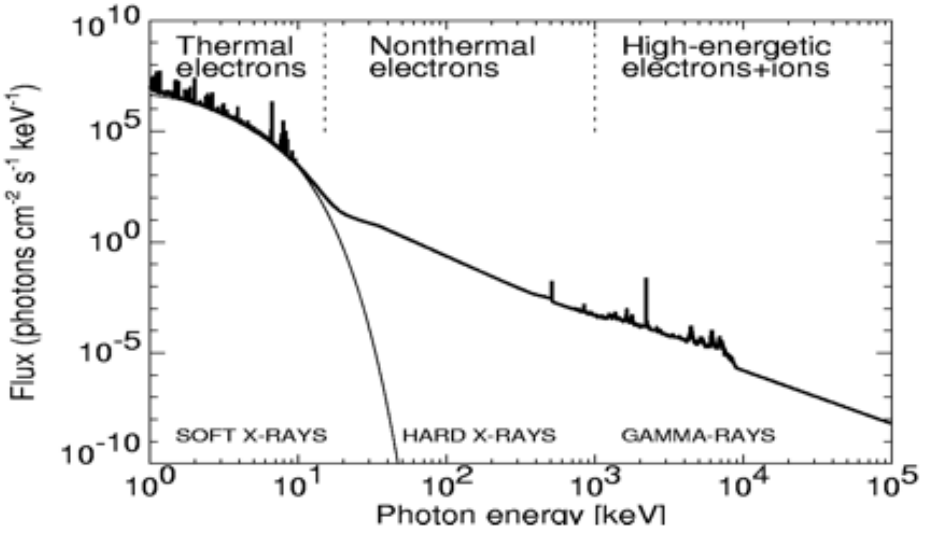

(1 eV $\approx$ 11,600 K $\approx 1.60 \times 10^{19}$ J)

And its interpretation:

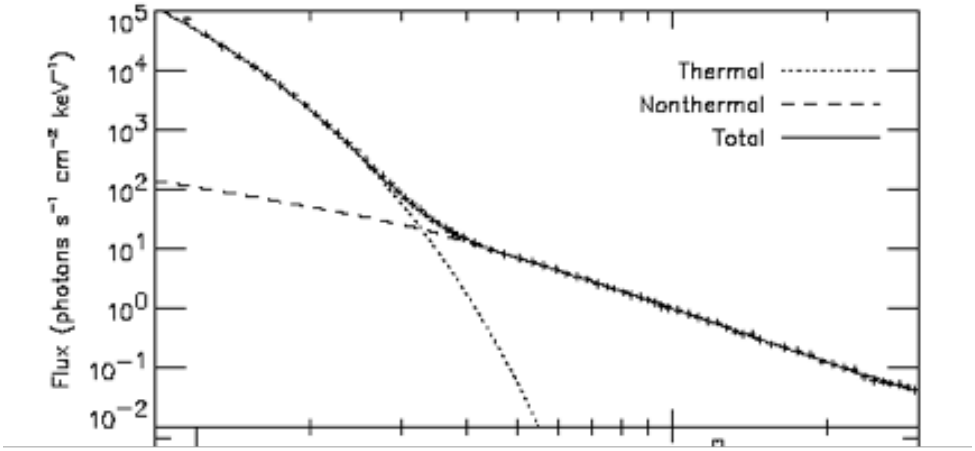

Typically, hard X-ray, gamma-ray and microwave light curves are very similar, as all these emissions are produced by the non-thermal electrons accelerated in the flare.

There is a relation between the soft X-ray flux (thermal emission) and hard X-ray and microwave fluxes (non-thermal emission): the **Neupert effect**. The Neupert effect simply notes that the hard X-rays occur during the rise phase of the soft X-rays.

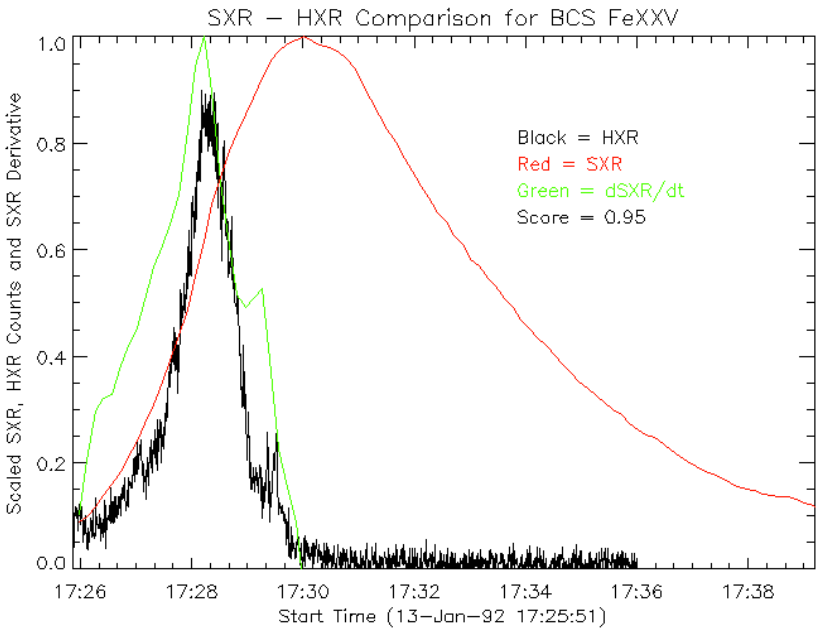

The time derivative of the soft X-ray light curve resembles the hard X-ray (and gamma-ray) light curve.

As the microwave emission has the time dependence very similar to the X-ray light curve, the Neupert effect is seen for the time dependence of the soft X-ray and microwave light curves too.

The standard model of solar flare:

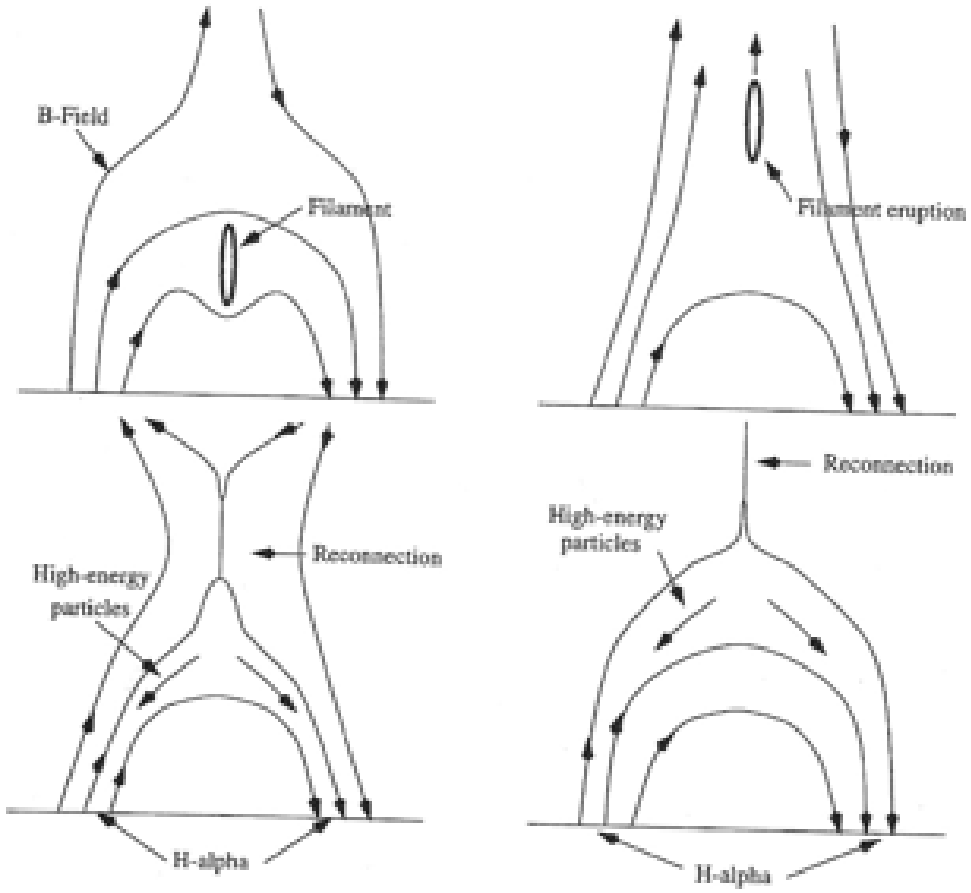

1. Magnetic free energy is stored in the corona, due to either motions of the photospheric footpoints of loops or to the emergence of current-carrying field from below the photosphere.
2. A cool, dense filament forms, suspended by the magnetic field, over the neutral line.
3. The field evolves slowly through equilibrium states, finally reaching a non-equilibrium which causes the closed field to rise and erupts outward.
4. The reconnection of the field below the rising filament provides plasma heating and particle acceleration that we call the flare.
5. The accelerated particles follow the field lines and interact with the chromosphere, heating it and causing the evaporation upflows of the plasma.
6. "Post-flare loops" (sometimes having a cusp-like shape) are formed over the neutral line; they gradually cool down by radiation.

7. More field lines are involved in reconnection; the reconnection site is going up, forming new post-flare loops situated above the previously created ones.
8. A multi-temperature arcade is formed with "older" cooler loops being below "new" hotter loops.

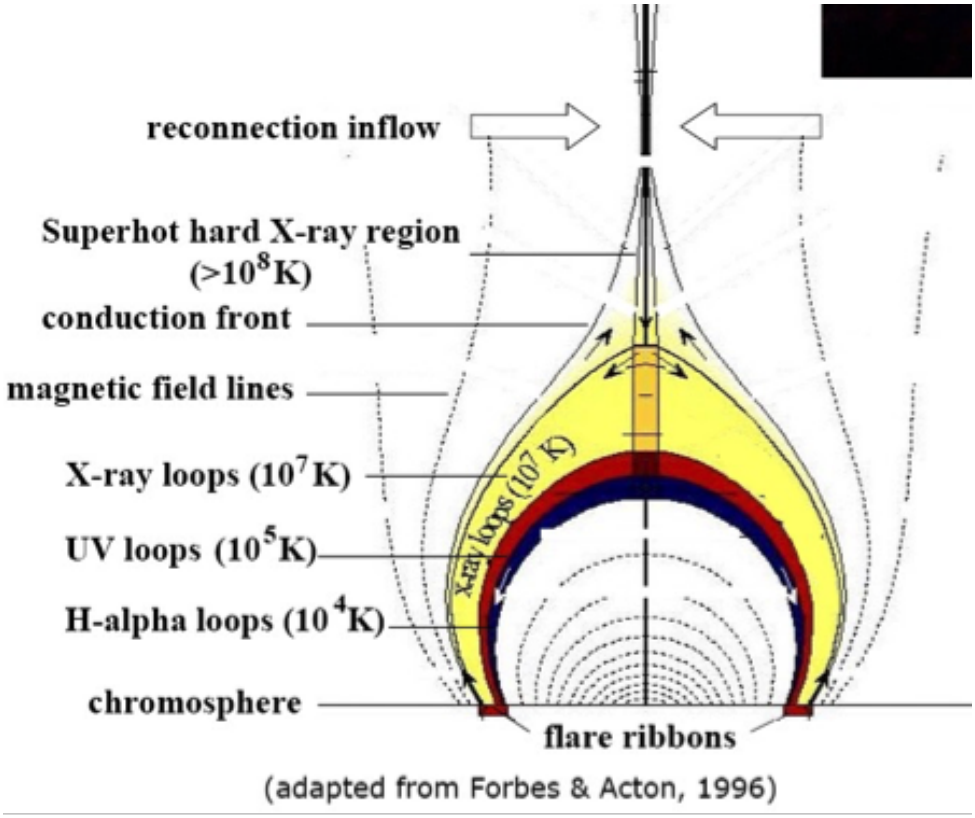

An observational detection of the cusp-like structure predicted by the standard solar flare model in soft X-rays:

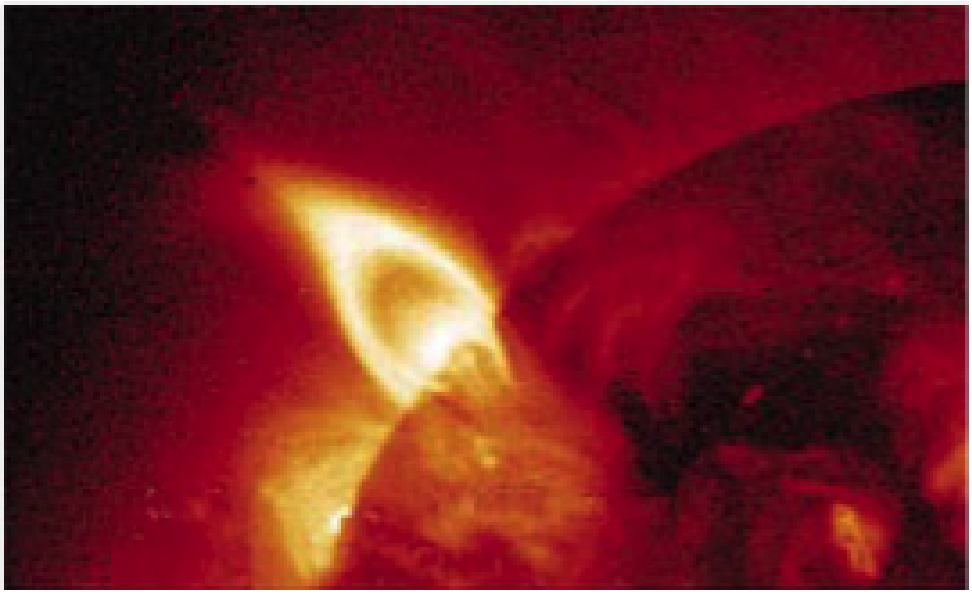

Emission associated with non-thermal electrons produced in the reconnection site:

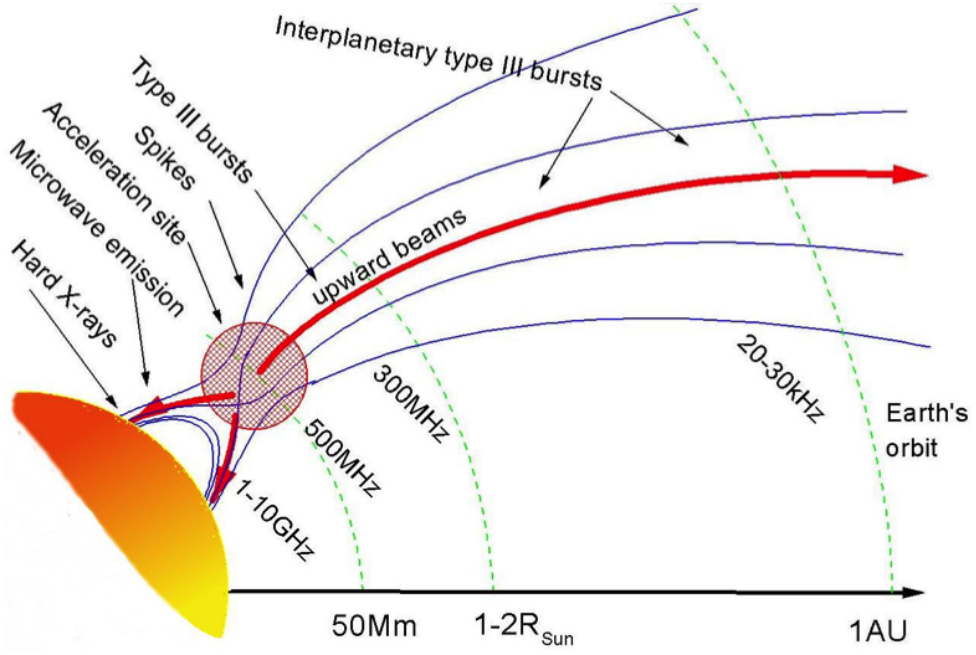

Spatial structure of the sources of soft X-ray (red contours) and hard X-ray (green contours) emission. The flaring loop (under the reconnection site) is seen in the soft X-rays, while the footpoints of this loop as seen in hard X-rays:

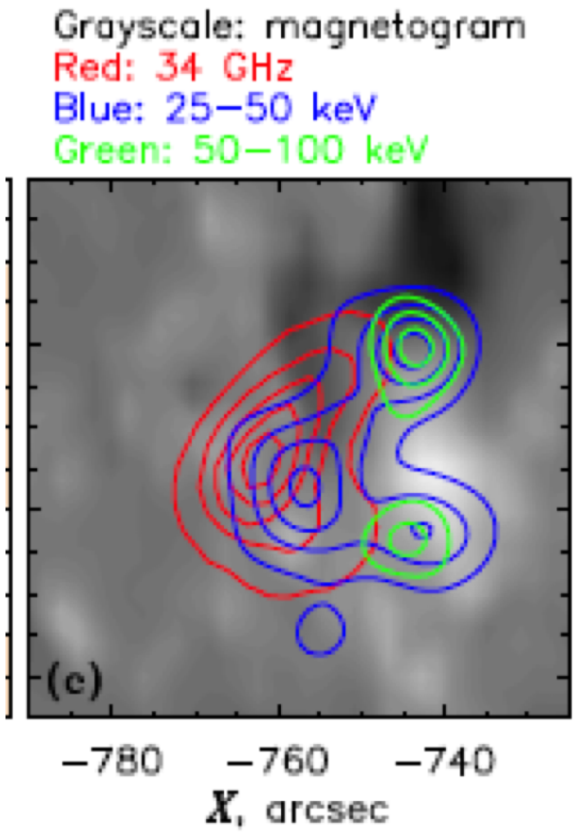

Thus, usually there are two hard X-ray sources in a flare. Gamma-ray sources have usually the same locations as the hard X-ray sources. Microwave emission is usually coming from the coronal part of the loop, where the non-thermal electrons accelerated by the flare emit the electromagnetic waves by the gyrosynchrotron mechanism:

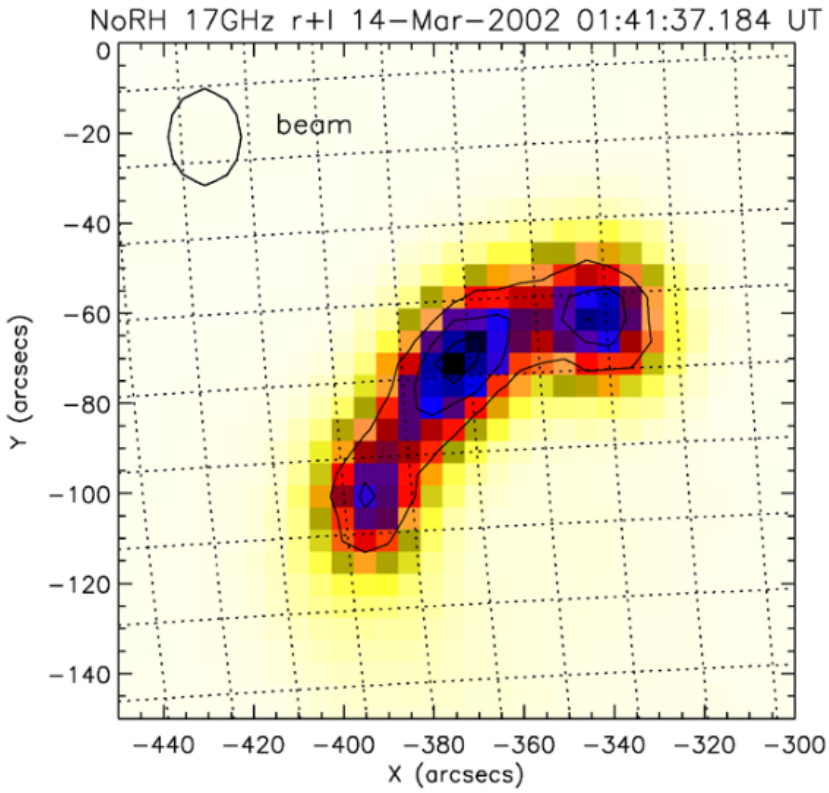

3D structure

Main morphological characteristics of flares according to the standard model: expanding ribbons over opposite-polarity magnetic fields and growing flare loops rooted in the ribbons connecting them. The shear angle of the flare loops decreases with time.

Example of a two-ribbon flare, the blue colour shows earlier times:

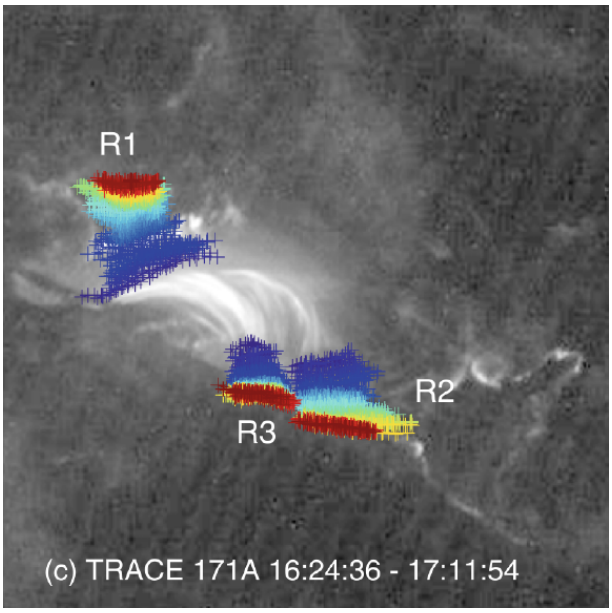

Another example of a two-ribbon flare. There the red colour shows the UV continuum, highlighting the footpoints of the arcade loops — the "ribbons":

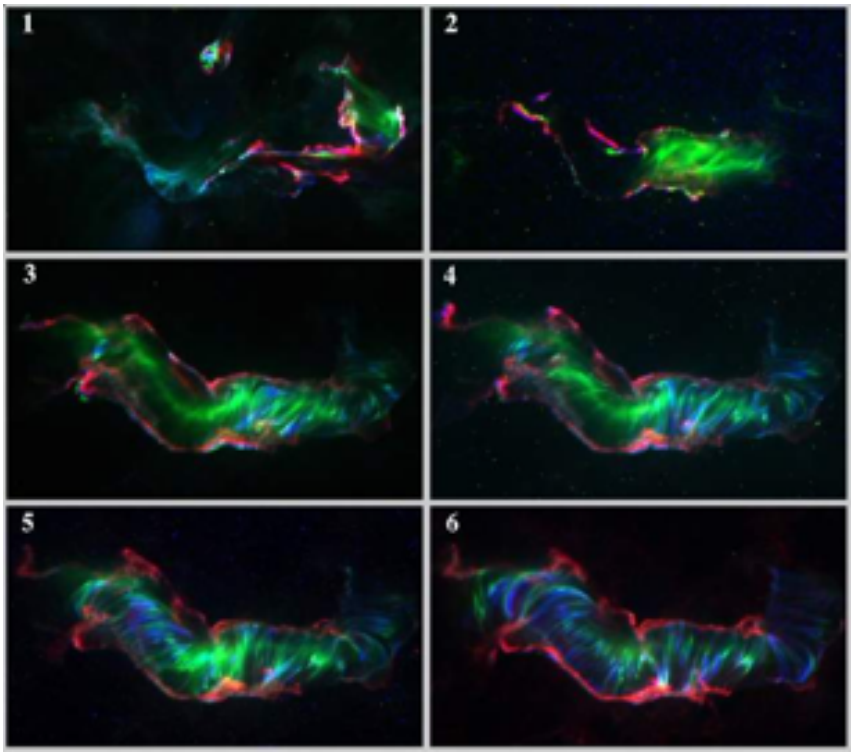

WL flare problem. The WL flare and strongest HXR patches are cospaNal, both being locaNons of intense energy deposition. They both form core patches of the UV flare ribbons in the close vicinity of magnetic inversion lines.

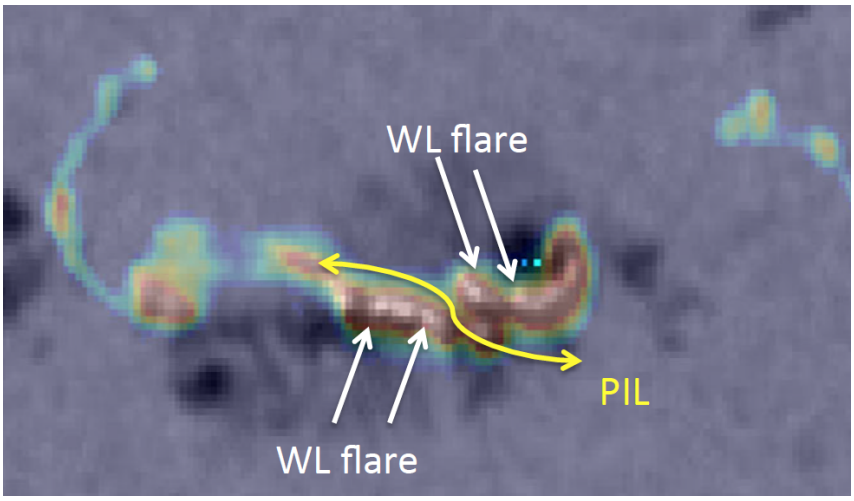

The mechanism responsible for the WL emission is flares is still not known,

but apparently it is associated with the precipitation of non-thermal electrons.

Another puzzle. Often the apparent ignition of the ribbons is seen to move along the neutral line:

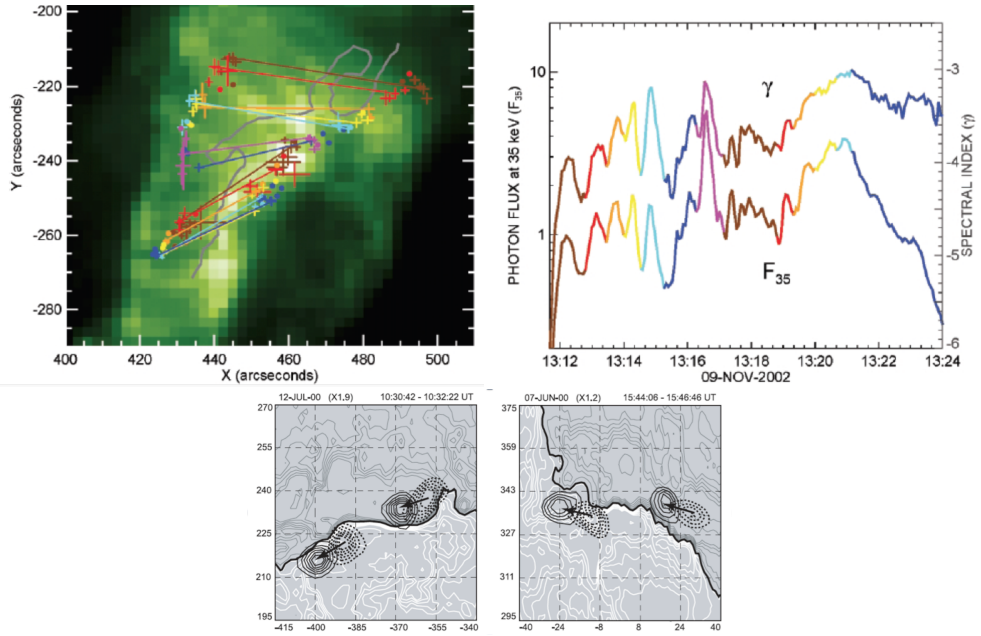

The speed of the apparent motion along the neutral line is 3–90 km/s. Often the motion is not steady, and consists of quasi-periodic pulsations.

Whipping-like and zipping-like asymmetric filament eruption models

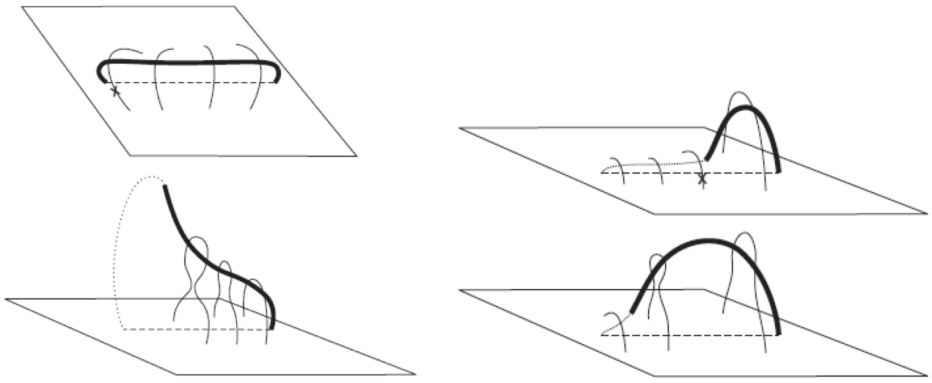

But why is the speed always so low?

There are other possible scenarios of solar flares, e.g.:

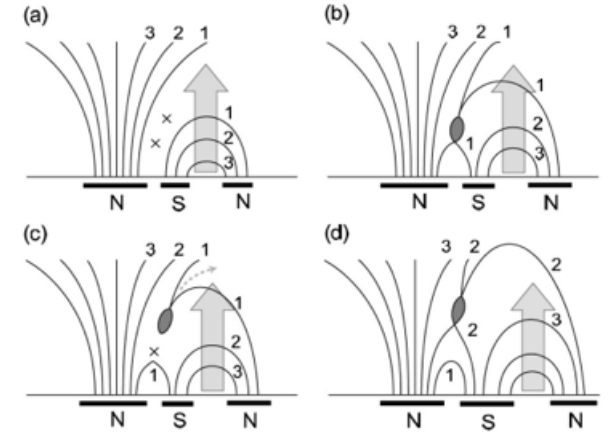

Statistics of solar flares

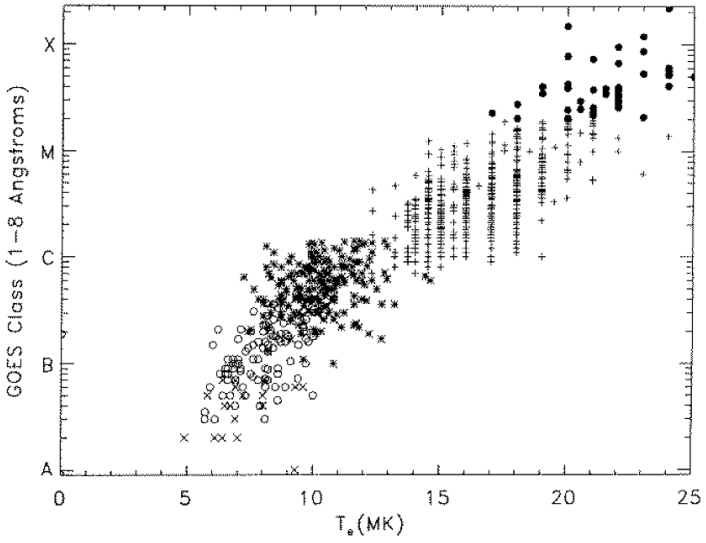

Scaling of the solar flare frequencies with different parameters of the flaring regions:

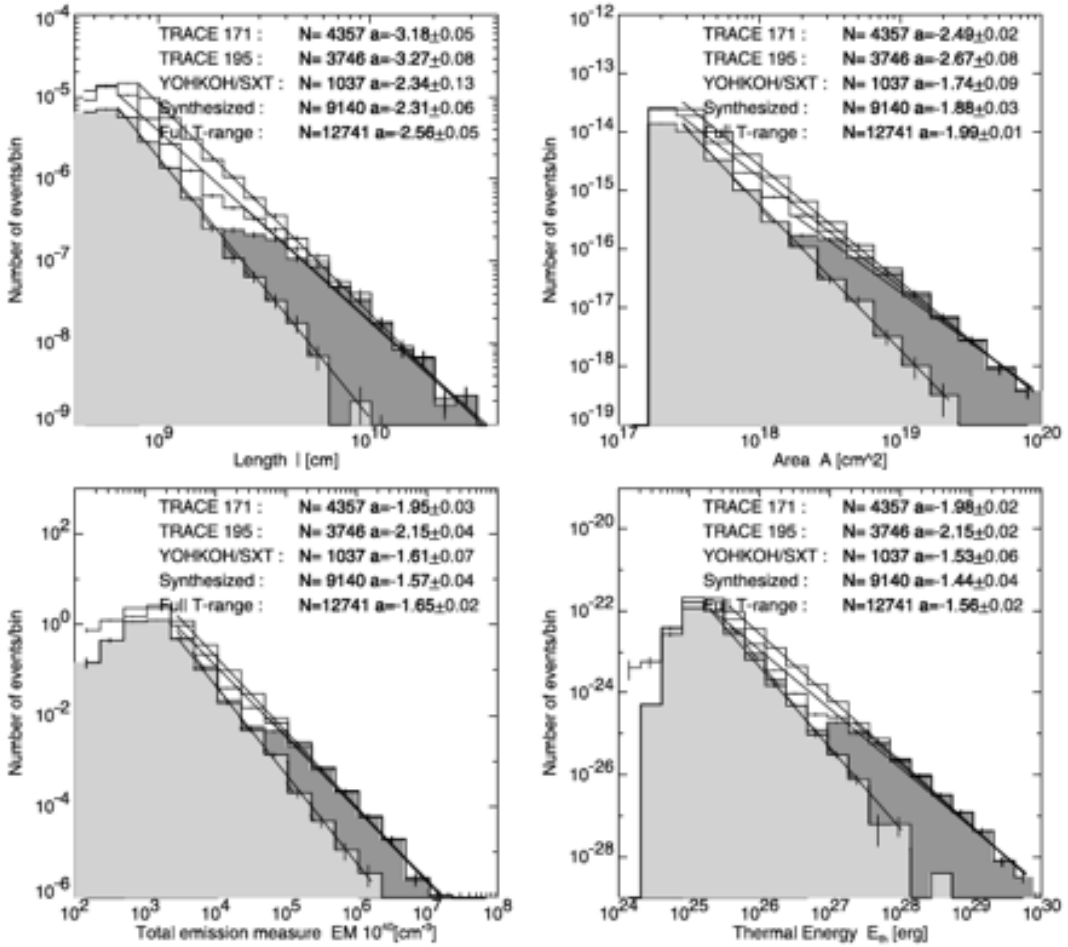

(Here the emission measure EM is the product of the electron concentration squared and the volume of the flaring site, so its dimension is m^{-3}.)

We see the power law distribution: the flare frequency f against its energy E: $f(E) \propto E^{-\alpha_{\mathrm{E}}}$.

The total heating rate released by all flares can be calculated by summing up the products of the flare frequencies $f(E)$ and energies over the range of possible energies:

$$W_{\mathrm{tot}} = \int_{E_{min}}^{E_{max}} f(E) E dE,$$

where $f(E) = f_0 (E/E_0)^{-\alpha_{\mathrm{E}}}$, and f_0 and E_0 are constant. Typically $E_{max} = 10^{32}$ erg, and $E_{min} = 10^{24}$ erg (so-called "nano-flares", while this value is still debated).

Evaluating the integral, obtain

$$W_{\rm tot} = \frac{f_0 E_0^2}{2-\alpha_{\rm E}} \left[\left(\frac{E_{max}}{E_0} \right)^{2-\alpha_{\rm E}} - \left(\frac{E_{min}}{E_0} \right)^{2-\alpha_{\rm E}} \right].$$

If $\alpha_{\rm E} < 2$, the bulk of heating is delivered by large events.
If $\alpha_{\rm E} > 2$, the bulk of heating is delivered by small events.

To compensate the energy losses by radiation and thermal conduction, the corona must be heated at the rate

- Active regions: $W_{\rm tot} \approx 10^7$ erg s^{-1} cm^{-2},
- Quiet corona: $W_{\rm tot} \approx 3 \times 10^5$ erg s^{-1} cm^{-2}.

Observational estimations of the power law index $\alpha_{\rm E}$:

Table 9.6: Frequency distributions of small-scale phenomena observed in quiet Sun regions.

Phenomenon	Number of events N	Powerlaw slope α_E	Energy range E_1, E_2 10^{24} [erg]	Total flux F [erg cm^{-2} s^{-1}]
EUV transients, EIT, 171+195[1]	233	2.45 ± 0.15	$10 - 300$	0.7×10^5
EUV transients, EIT 195[2]	228	1.35 ± 0.20	$1 - 100$	...
EUV transients, EIT 195[3]	277	1.45 ± 0.20	$10 - 100$	...
Nanoflares, TRACE, 171+195[4]	5131	2.48 ± 0.11	$0.3 - 60$	0.2×10^5
Nanoflares, TRACE+SXT[5]	281	1.53 ± 0.02	$10 - 10^6$	0.5×10^5
Blinkers, CDS, O V[6]	790	1.34 ± 0.08	$0.01 - 0.3$	...
Explosive ev., SUMER C III[7]	3403	2.8 ± 0.1	$0.05 - 2$	0.45×10^5
Explosive ev., SUMER Ne IV[7]	2505	2.8 ± 0.1	$0.6 - 10$	0.16×10^5
Explosive ev., SUMER O VI[7]	5531	3.3 ± 0.4	$0.1 - 2$	0.79×10^5
Explosive ev., SUMER Ne VIII[7]	2907	2.8 ± 0.5	$0.06 - 1$	0.03×10^5

[1] Krucker & Benz (1998); [2] Berghmans et al. (1998); [3] Berghmans & Clette (1999); [4] Parnell & Jupp (2000) [corrected for a factor of 100 in original paper]; [5] Aschwanden et al. (2000b); [6] Brkovic et al. (2001); [7] Winebarger et al. (2002).

The detected radiation of the EUV and SXT nanoflares roughly corresponds to a third of the total coronal heating requirement. Hence the coronal heating problem remains unsolved.

Variation of the emitted X-ray flux with solar cycle:

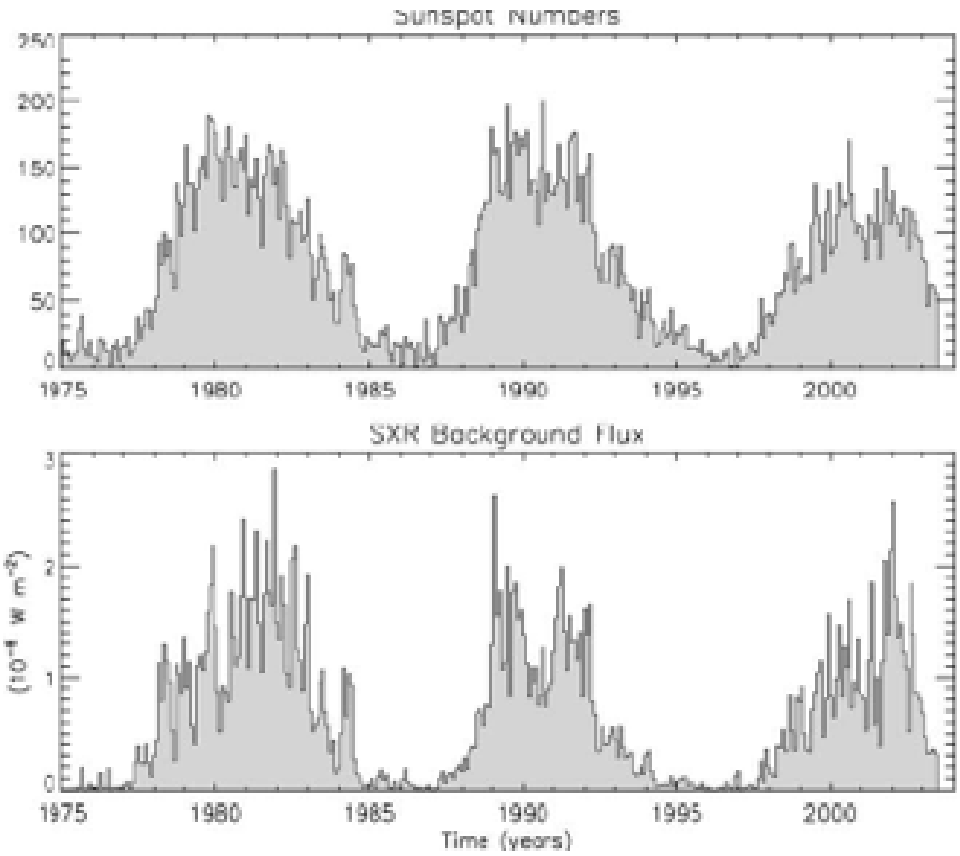

Correlation of emitted X-ray flux with sunspot numbers:

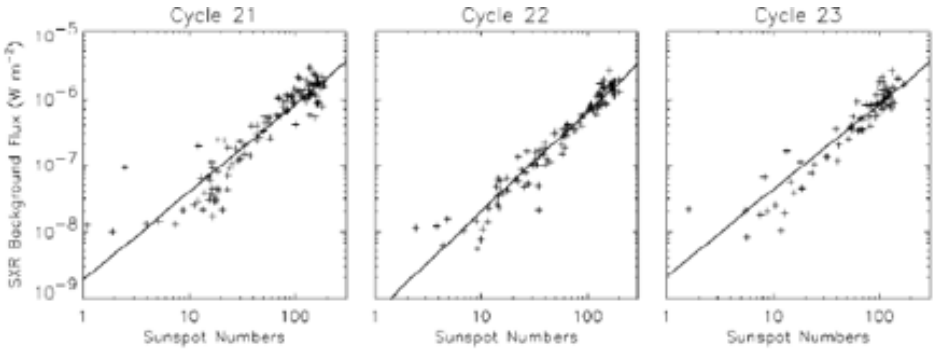

Super- and megaflares on stars:

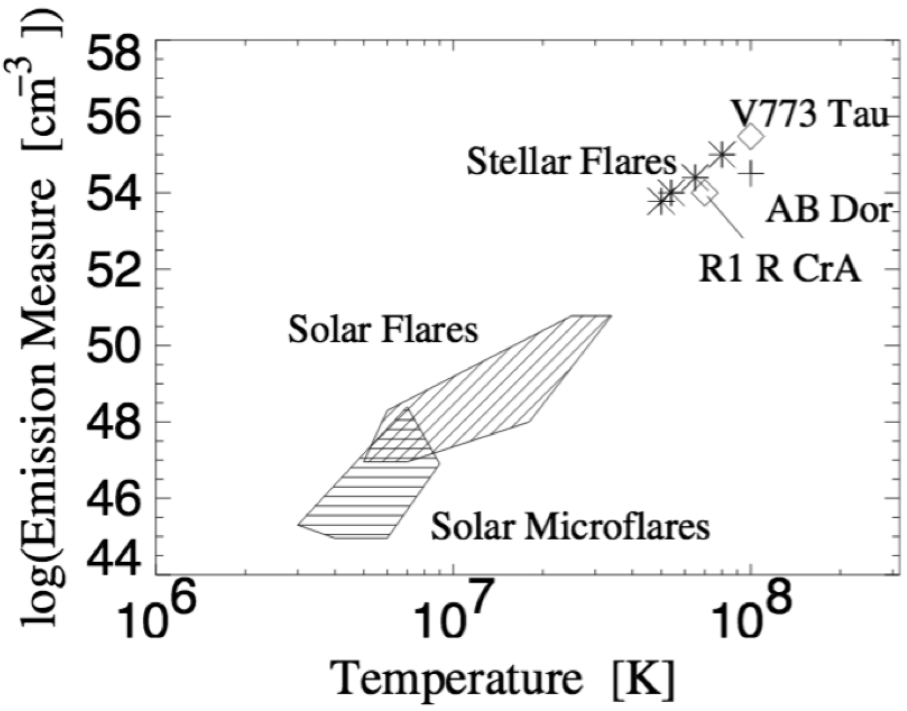

FIG. 1.—The log-log plot of EM vs. electron temperature of solar flares (from Feldman et al. 1995), solar microflares observed by *Yohkoh* SXT (from Shimizu 1995), four stellar flares (*asterisks*; from Feldman et al. 1995), a protostellar flare (*diamond*; class 1 protostar far-IR source R1 in the R CrA cloud; from Koyama et al. 1996), a T Tauri stellar flare (*diamond*; weak-lined T Tauri star V773 Tau; from Tsuboi et al. 1998), and a stellar flare on AB Dor (K0 IV zero-age main-sequence single star) by *BeppoSAX* (*plus sign*; Pallavicini 2001).

Do solar flares and stellar superflares are produced by similar mechanisms?

Initiation of CMEs

CMEs (first observed in 1971?) are thought to be catastrophic disruptions of the force balance between the upward magnetic pressure of the filament and the downward tension of the overlying field.

• CME is a counter-intuitive process, when a large amount of plasma is being limed up by invisible forces defying the Suns gravity.
• There is a perpetual competition between increasingly non-potential magnetic fields trying to find a new equilibrium through expansion and restraining forces exerted by magnetic tension in overlying magnetic fields.
• CME can be initiated by an increase of internal shear/twist or a decrease/removal of restraining magnetic tension acting like tethers.

Flare-CME timing:

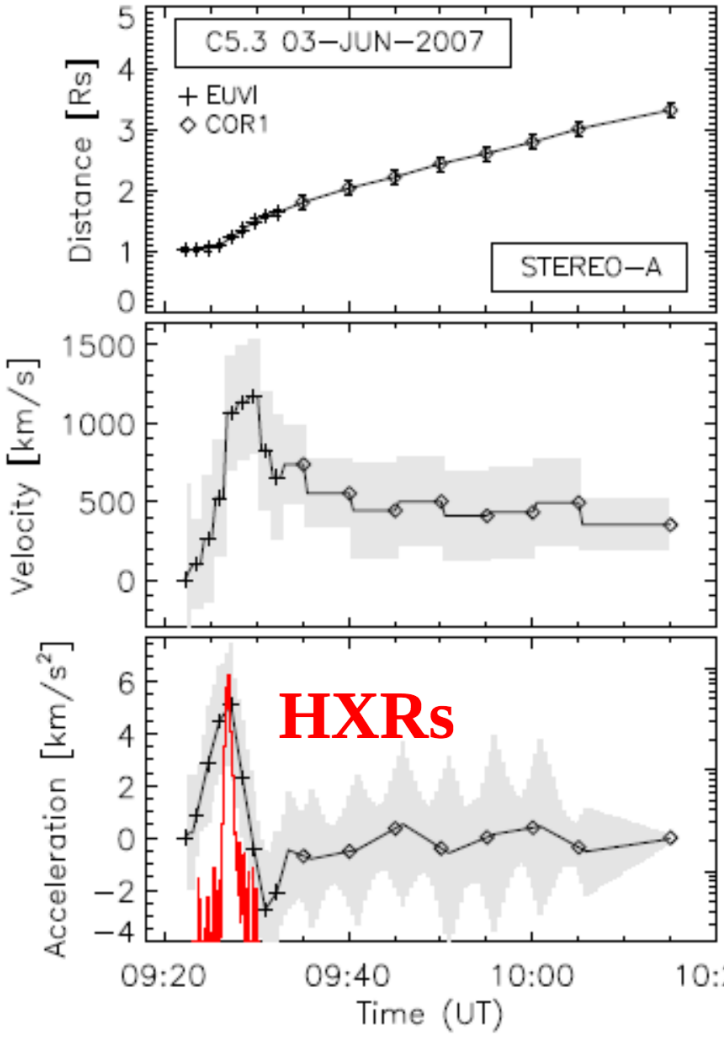

CMEs are observed to have acceleration, deceleration or constant speed.

A combined CME–flare model:

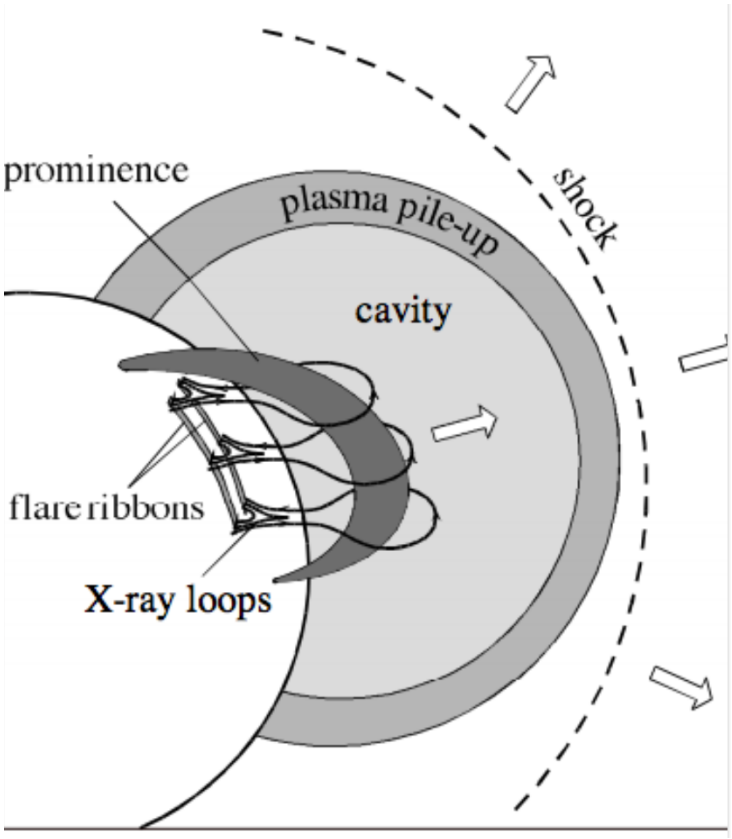

Flux Rope Formation by Reconnection:

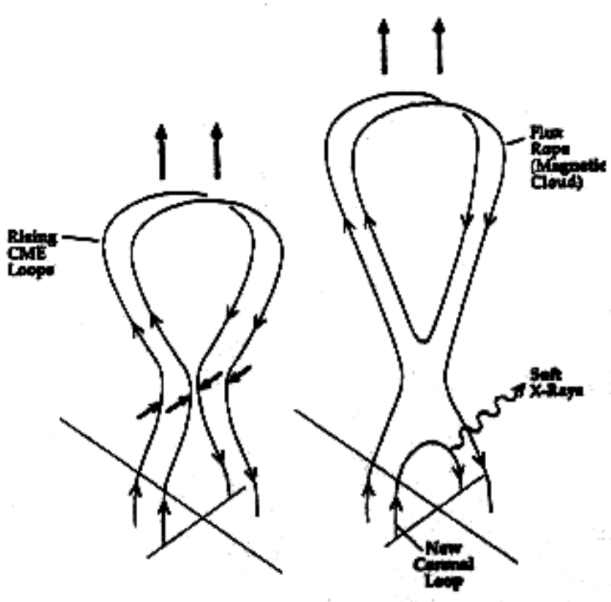

Kink and torus instabilities models:

Torus instability is driven by the *hoop* force (gradient of the magnetic pressure $B^2/2\mu_0$) in a semi-circular flux rope:

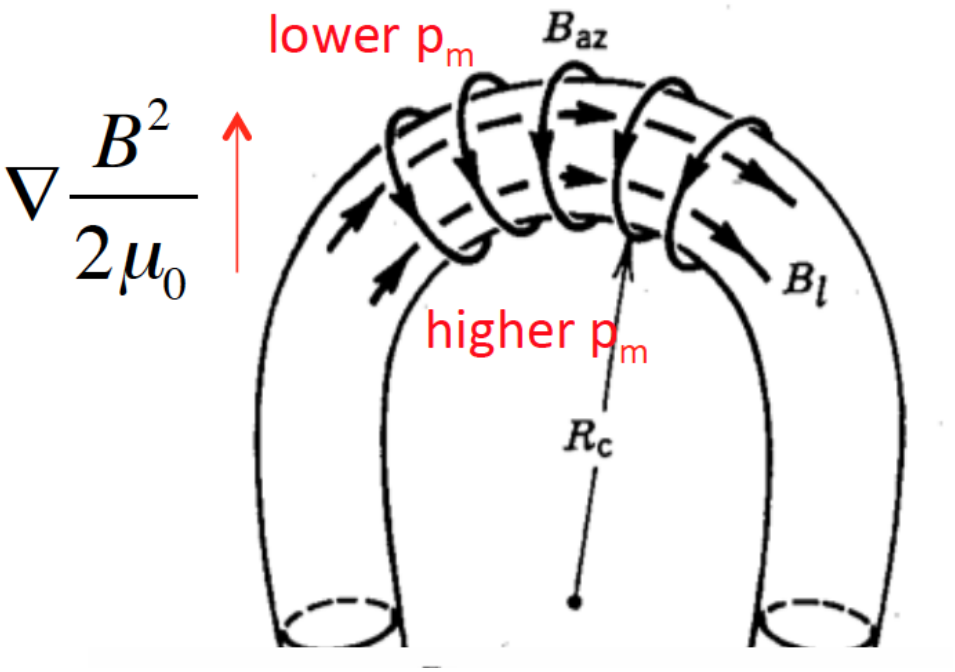

- In a loop-like curved magnetic flux rope there is an imbalance between axial and azimuthal fields: The loop's curvature packs the azimuthal field lines together more densely at the inner edge, so the azimuthal field (associated with the twist in the loop) will be more intense at the inner edge of the loop apex than at the outer.
- The resulting gradient of the magnetic pressure $\nabla(B^2/2\mu_0)$ will tend to expand the loop outward against the tensions of the axial field lines.
- In equilibrium, the difference of these two forces must be balanced by downward acceleration of gravity on the plasma contained in the rope and the tension and magnetic pressure gradients of the overlying field.
- Instability could set in when equilibrium is lost due to changes in the fields.

If there is significant twist in the rope:

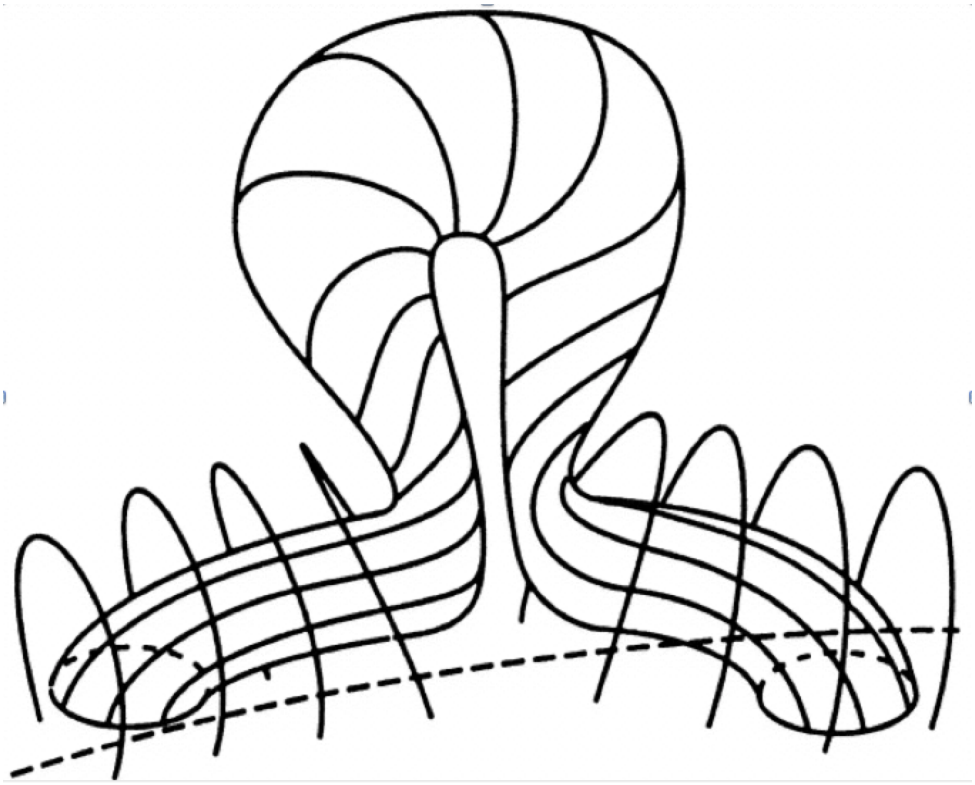

Flare-related magnetic reconnection under the rising flux rope further increases the poloidal flux of the flux rope, increasing the hoop force driving it upward.

Summary of CME models:

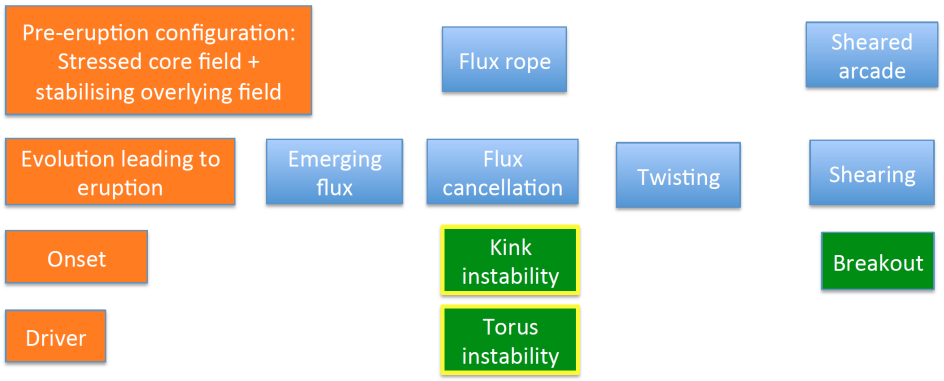

As the sheared arcade is converted into a flux rope during the eruption, all CME models at some stage will have a flux rope; CMEs are increasingly modelled as erupting flux ropes.

There are two general topological approaches related to CME initiation:
- 1. Sheared arcade - an array of magnetic loops following magnetic neutral lines (the top of a flux rope that has not fully emerged into the solar atmosphere)
- 2. Twisted flux tube (flux rope) - a coherent toroidal magnetic structure with field-lines wound around a major axis.
Amount of twist critical for CME initiation models (high threshold).

Flux Cancellation Models (magnetic rope formation — build-up of sigmoids):

• Flux cancellation is the disappearance of magnetic fields of opposite polarity at the neutral line separating them.
• Flux cancellation at the neutral line of a sheared arcade causes the flux rope that supports prominence material.
• Equilibrium breaks down if flux cancellation continues after the flux rope is formed.
• A new equilibrium forms farther out.
• The solar wind pulls the flux rope out and forms a current sheet at which reconnection occurs.

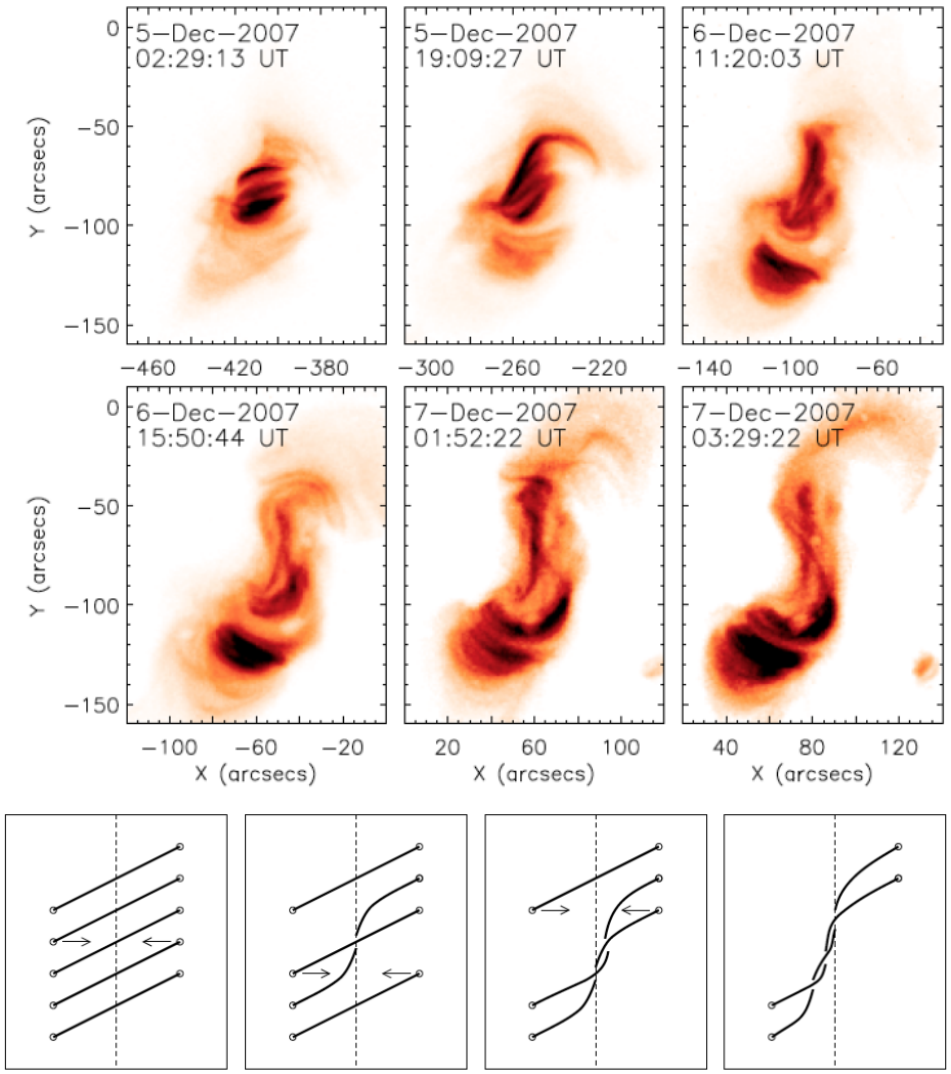

In this scenario, formation of flux rope happens **before** eruption.

Breakout model: • Breakout CME: quadrupolar field, sheared at central neutral line;
• Reconnection in front of CME removes confining field and allows it to erupt;
• As in flux cancellation models, reconnection behind CME cuts field lines connecting to the Sun, creating flux rope **after** eruption.

All models produce a current sheet under the erupting flux rope, and a flare.

Kelvin-Helmholtz instability in a CME.

Formation of a vortex street at a CME flank:

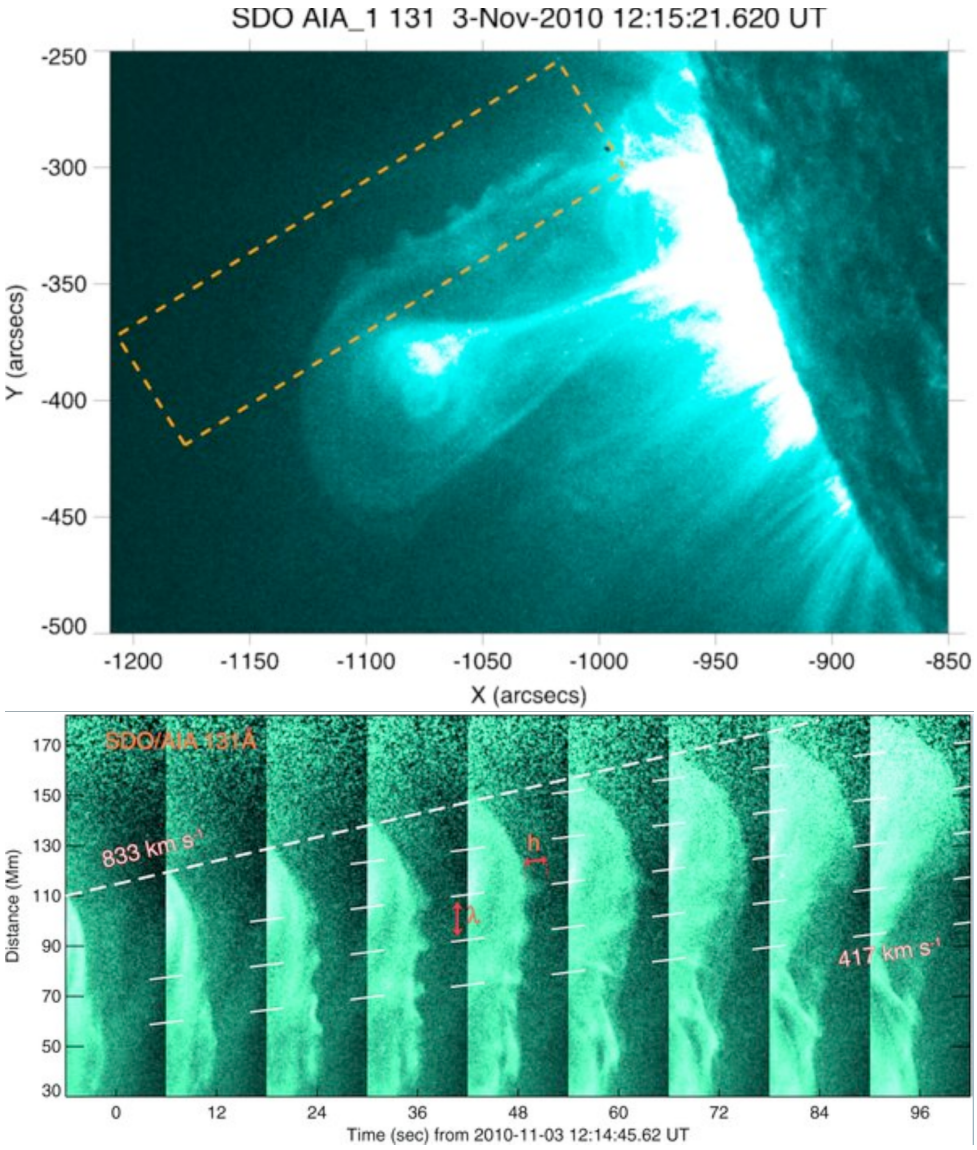

- Typical size of the vortex: 10 Mm, developed in about 30 s.
- The increment is 0.05–0.03 s^{-1}.
- Miura (1984): the increment is $0.1 V_{\text{ejecta}} \Delta L$.
- Sound speed: 504 km s^{-1} at 11 MK.
- Alfvén speed < 918 km s^{-1} — quite possible.
- As the fastest growing KH modes is known to occur at wavelength approximately 6–12 ΔL, we deduce that $\Delta L \approx 2 - 3$ Mm.

The formation of KH vortices leads to the **aerodynamic drag force**, that determines the CME kinematics:

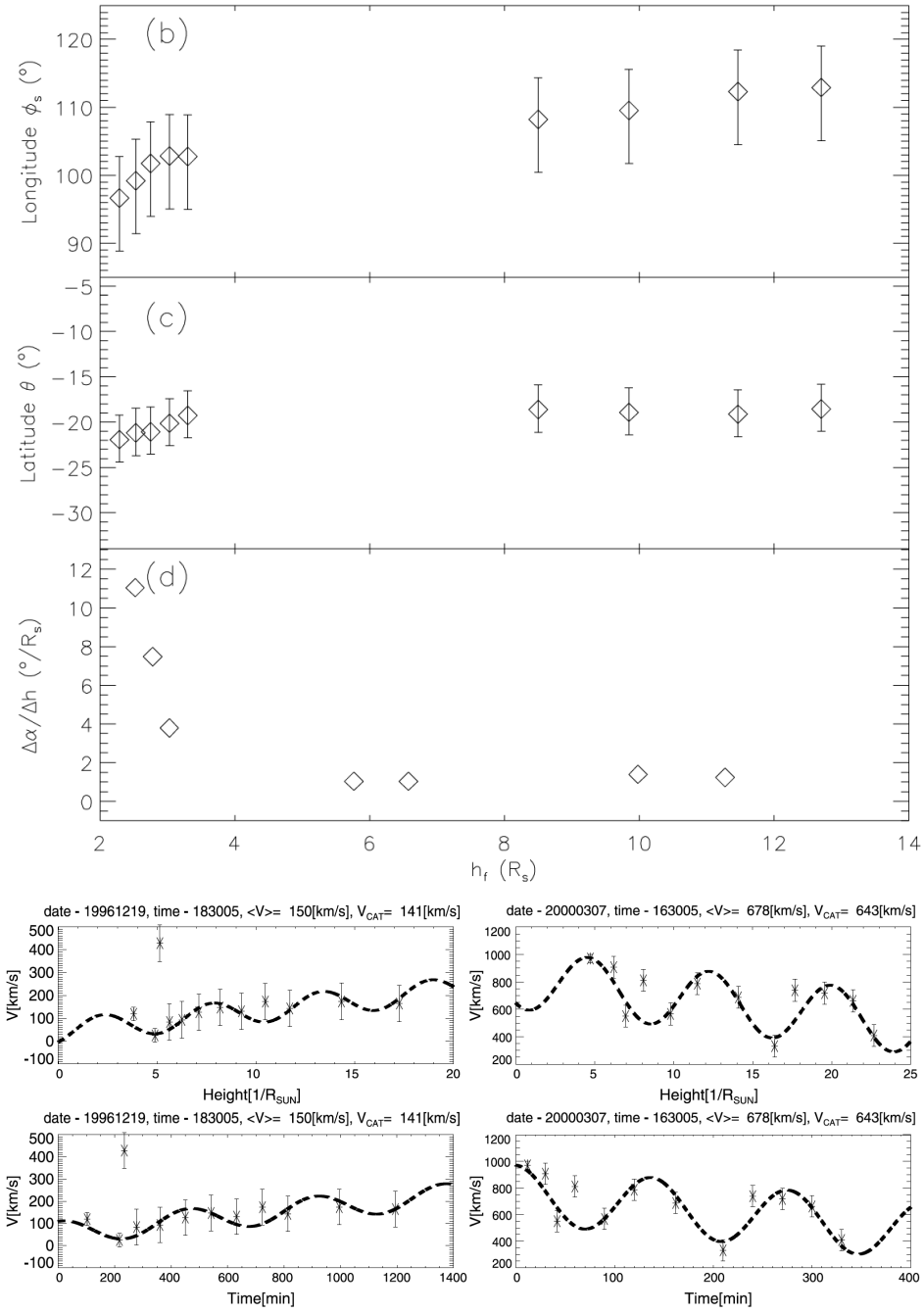

Another process that affects the CME arrival time is the interaction of the CME with Parker's spiral:

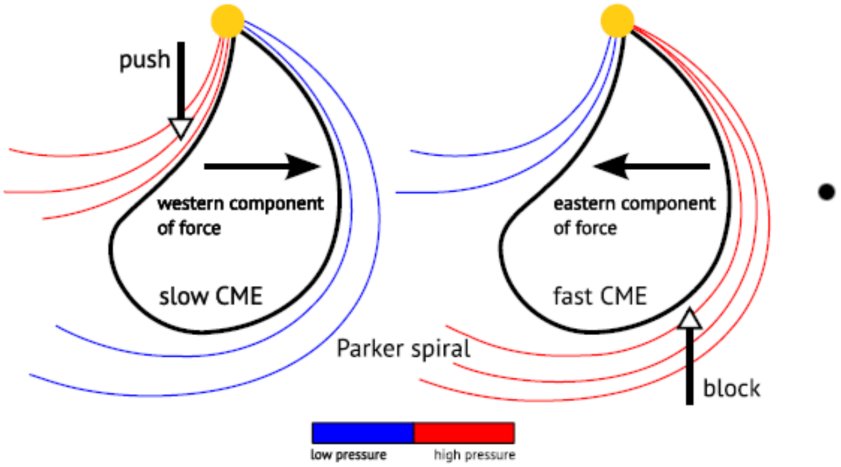
push
western component
of force
slow CME
eastern component
of force
fast CME
Parker spiral
block
low pressure
high pressure